Supplementary Information

Highly Conductive Paper/Textile Electrodes Using Ligand Exchange Reaction-Induced in-situ Metallic Fusion

Sungkun Kang, Donghyeon Nam, Jimin Choi, Jongkuk Ko, Donghee Kim, Cheong Hoon Kwon, June Huh, and Jinhan Cho*

Department of Chemical & Biological Engineering, Korea University, 145 Anam-ro, Seongbuk-gu, Seoul 02841, Republic of Korea.

*Address correspondence to jinhan71@korea.ac.kr.

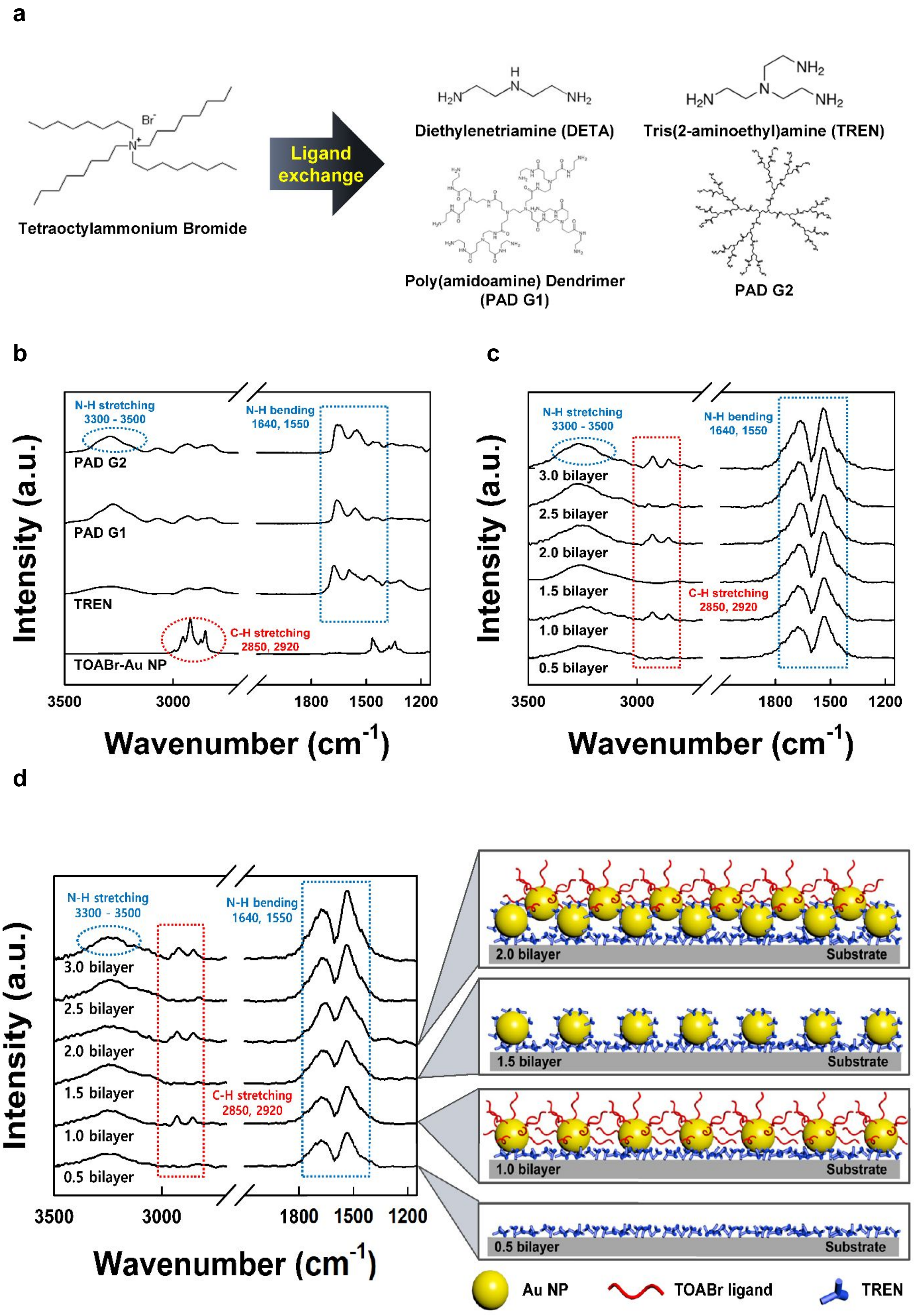
a
Tetraoctylammonium Bromide
Br-
N+
Ligand exchange
H
N
H2N
NH2
Diethylenetriamine (DETA)
NH2
N
H2N
NH2
Tris(2-aminoethyl)amine (TREN)
Poly(amidoamine) Dendrimer (PAD G1)
PAD G2
b
N-H stretching 3300 - 3500
N-H bending 1640, 1550
PAD G2
PAD G1
TREN
TOABr-Au NP
C-H stretching 2850, 2920
Intensity (a.u.)
3500
3000
1800
1500
1200
Wavenumber (cm-1)
c
N-H stretching 3300 - 3500
N-H bending 1640, 1550
C-H stretching 2850, 2920
3.0 bilayer
2.5 bilayer
2.0 bilayer
1.5 bilayer
1.0 bilayer
0.5 bilayer
Intensity (a.u.)
3500
3000
1800
1500
1200
Wavenumber (cm-1)
d
N-H stretching 3300 - 3500
N-H bending 1640, 1550
C-H stretching 2850, 2920
3.0 bilayer
2.5 bilayer
2.0 bilayer
1.5 bilayer
1.0 bilayer
0.5 bilayer
Intensity (a.u.)
3500
3000
1800
1500
1200
Wavenumber (cm-1)
2.0 bilayer
Substrate
1.5 bilayer
Substrate
1.0 bilayer
Substrate
0.5 bilayer
Substrate
Au NP
TOABr ligand
TREN

Figure S1. (a) Molecular structures of TOABr, DETA,TREN, PAD-G1, and PAD-G2. (b) FTIR spectra of PAD-G2, PAD-G1, TREN, and TOABr-Au NPs. (c) ATR-FTIR spectra of (PAD-G1/TOABr-Au NP)$_n$ and (d) (TREN/TOABr-Au NP)$_n$ multilayers as a function of the bilayer number (n). In this case, the C-H stretching peaks at 2850 and 2920 cm^{-1} originate from long alkyl chains of TOABr ligands, and on the other hand, the N-H stretching (at 3300-3500 cm^{-1}) and the N-H bending peaks (at 1640 and 1550 cm^{-1}) occur from amine groups of PAD-G1 or TREN. The scheme shown in the right side of (d) displays LbL assembly process based on ligand exchange reaction between TOABr and TREN.

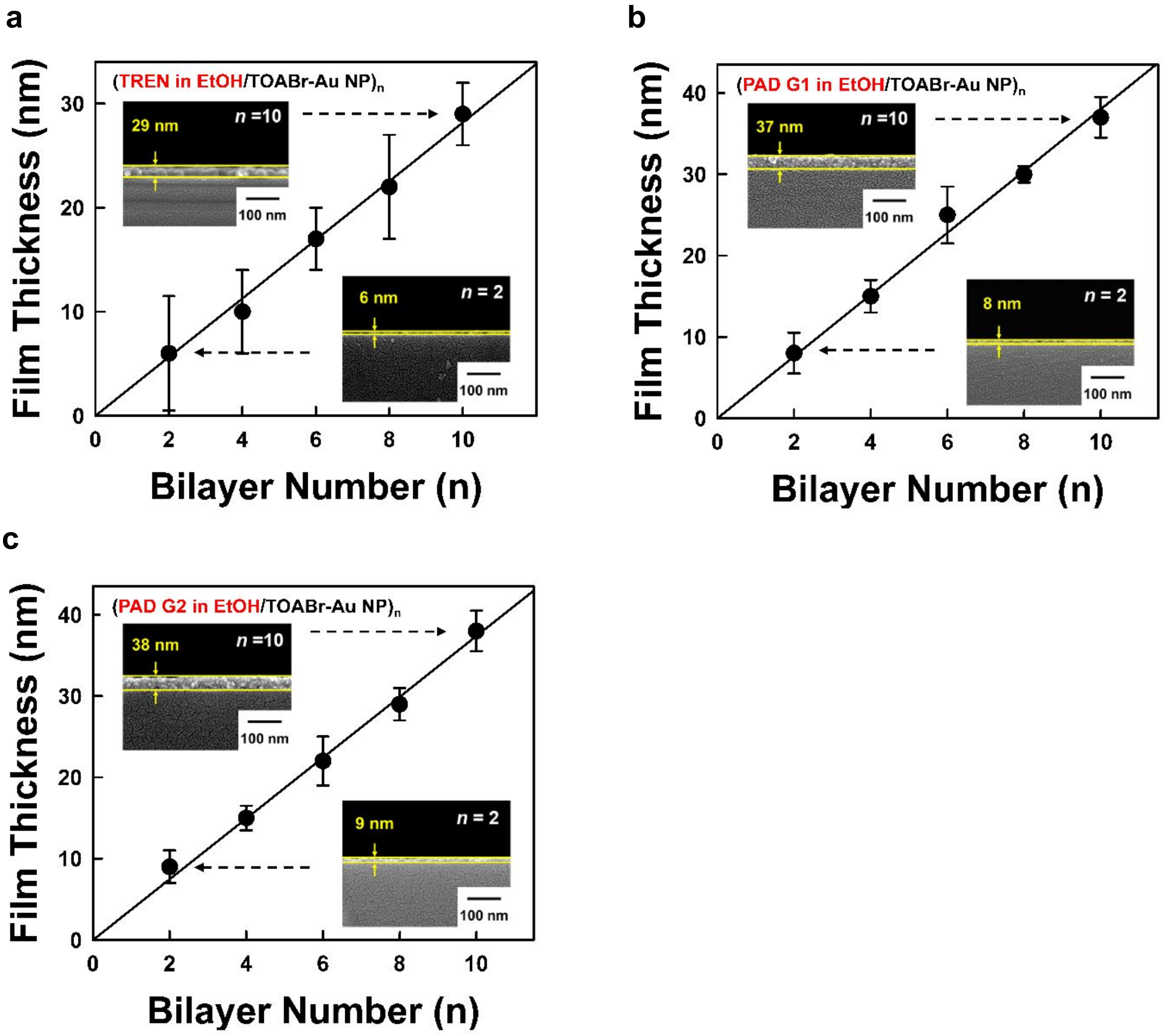

Figure S2. Total thicknesses of (a) (TREN/TOABr-Au NP)$_n$, (b) (PAD-G1/TOABr-Au NP)$_n$, and (c) (PAD-G2/TOABr-Au NP)$_n$ multilayers as a function of the bilayer number (n). The insets show the cross-sectional FE-SEM images of multilayers.

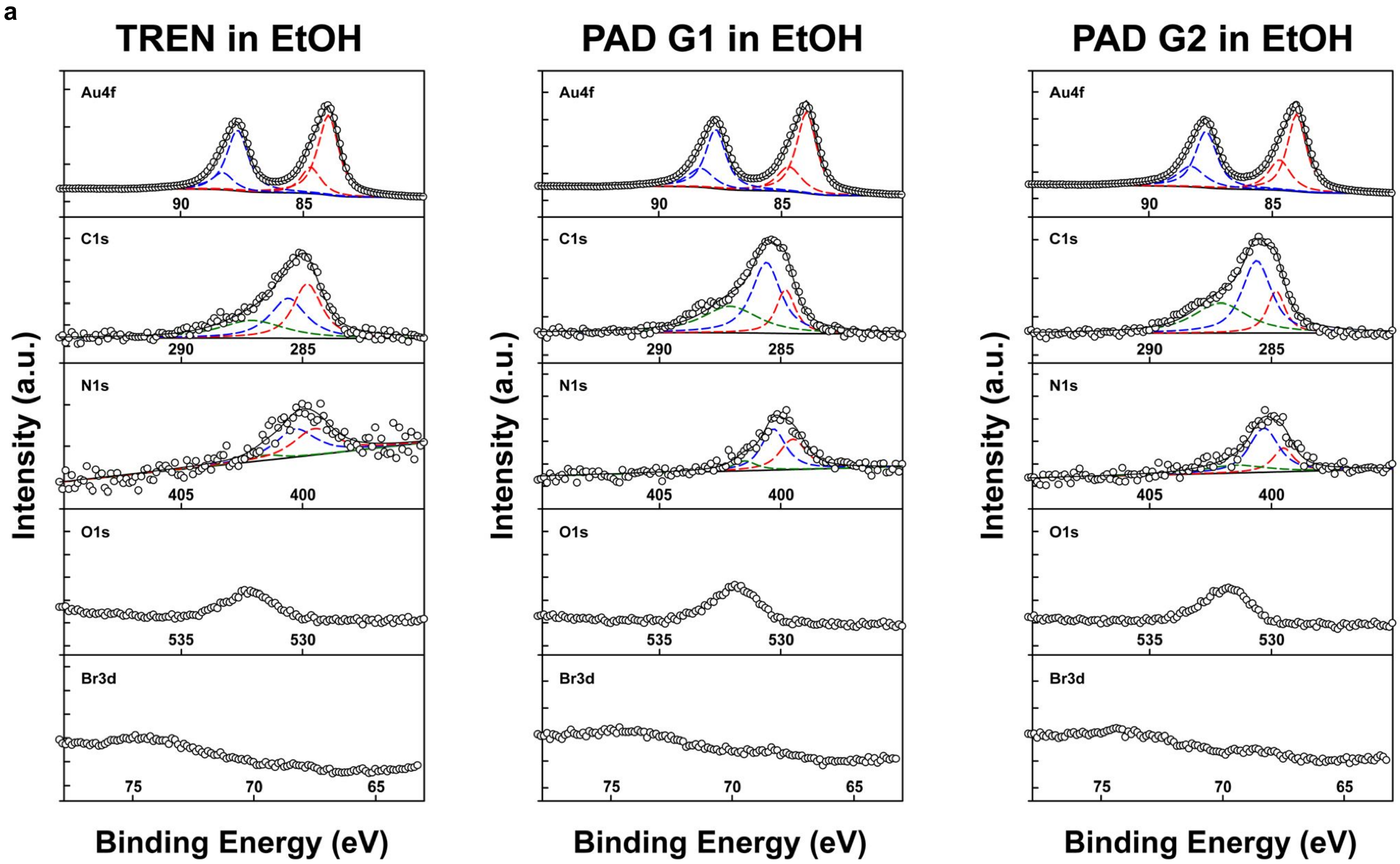
a
TREN in EtOH
PAD G1 in EtOH
PAD G2 in EtOH
Au4f
C1s
N1s
O1s
Br3d
90
85
290
285
405
400
535
530
75
70
65
Intensity (a.u.)
Binding Energy (eV)

b

	Elements	Au4f 7/2		Au4f 5/2		C1s			N1s			O1s	Br3d
	Phase	Au	Au-N	Au	Au-N	C-C	C-N	C-N^+	N-C	N^+-C	N-Au		
Linker	B.E (eV)	83.9	84.7	87.6	88.3	284.8	285.6	287.1	399.5	400.3	401.5	532.0	-
TREN	ar (%)	18.97	5.98	14.99	4.26	13.36	12.53	9.91	3.29	3.48	0.43	10.0	2.8
PAD G1	ar (%)	10.99	4.11	8.18	3.32	9.42	23.64	17.34	3.97	4.68	1.15	12.4	0.7
PAD G2	ar (%)	10.01	4.66	8.20	3.93	8.29	22.98	18.13	2.54	6.36	2.40	11.8	0.8

c

	TREN	**PAD G1**	**PAD G2**
Mass ratio of Au (%)	90.5	84.0	84.0

Figure S3. (a) XPS spectra, (b) atomic ratios, and (c) mass ratio analysis of (TREN/TOABr-Au NP)$_{10}$, (PAD-G1/TOABr-Au NP)$_{10}$, and (PAD-G2/TOABr-Au NP)$_{10}$ multilayers deposited onto Si wafers. Mass ratios were calculated from multiplying the atomic mass by the atomic ratio.

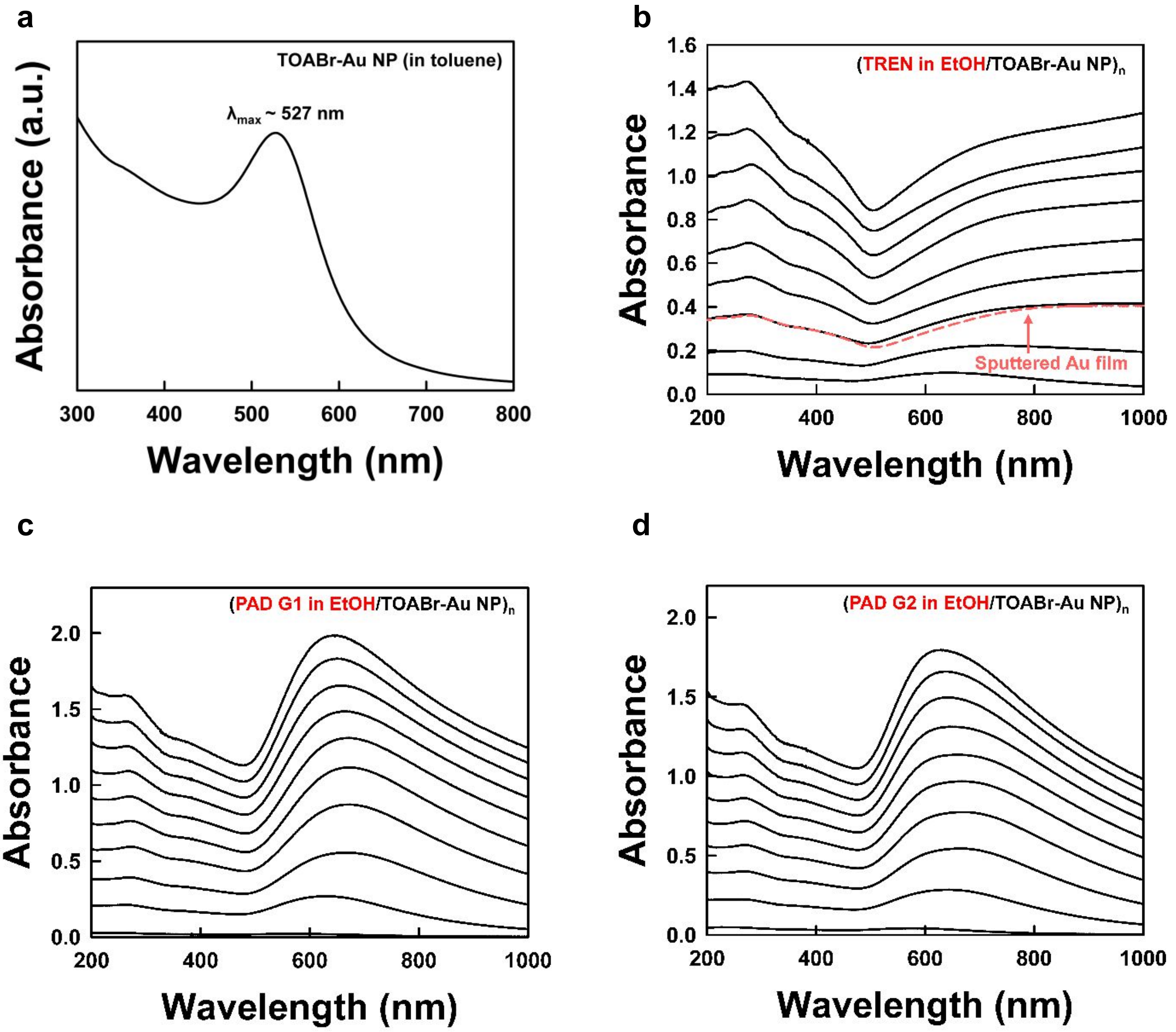

Figure S4. UV-vis spectra of (a) TOABr-Au NPs in toluene, (b) (TREN/TOABr-Au NP)$_n$, (c) (PAD-G1/TOABr-Au NP)$_n$, and (d) (PAD-G2/TOABr-Au NP)$_n$ multilayers as a function of the bilayer number (n).

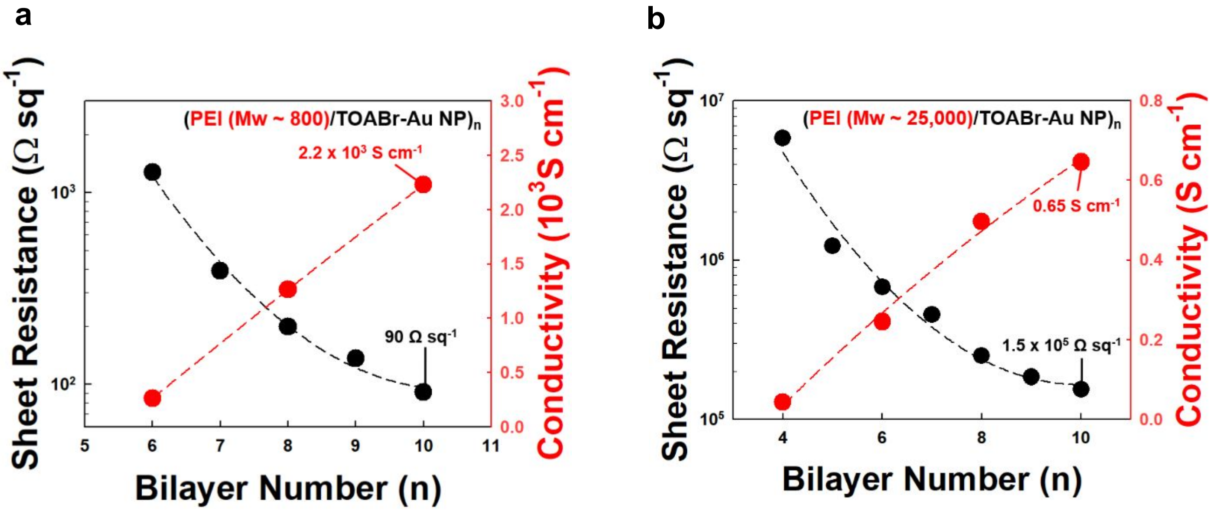

Figure S5. Electrical Conductivity of (a) (PEI (M_w ~ 800)/TOABr-Au NP)$_n$ and (b) (PEI (M_w ~ 25,000)/TOABr-Au NP)$_n$ multilayers as a function of bilayer number (n).

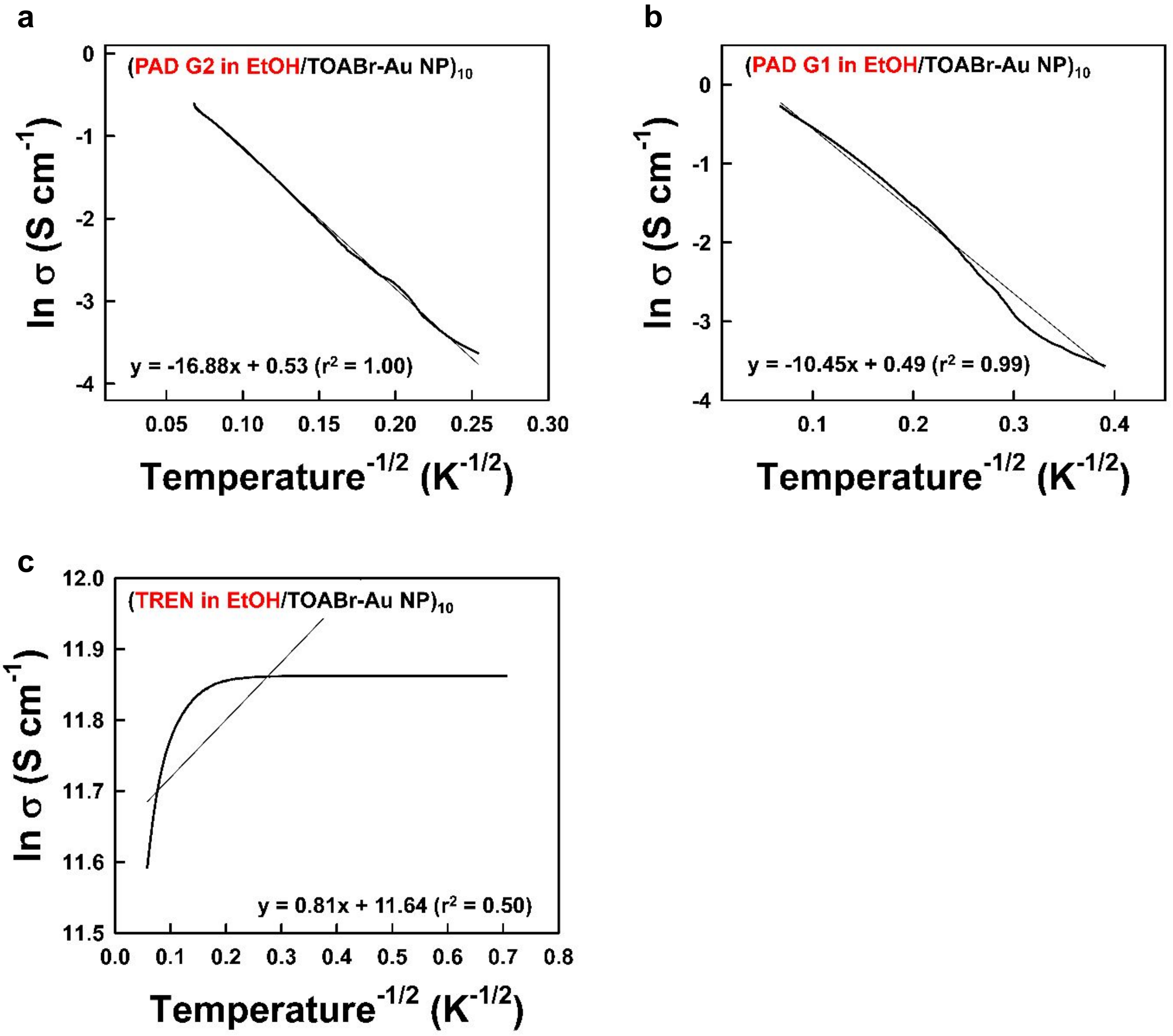

Figure S6. Plot of *lnσ vs* $T^{-1/2}$ for the tunneling mechanism of (a) (PAD-G2/TOABr-Au NP)$_{10}$, (b) (PAD-G1/TOABr-Au NP)$_{10}$, and (c) (TREN/TOABr-Au NP)$_{10}$ multilayer films. In the case of Figure S5c, the conductivity ($ln\ \sigma$) as a function of $T^{-1/2}$ (for hopping) for the (TREN/TOABr-Au NP)$_{10}$ multilayers do not correspond to a linear dependence, suggesting metallic conduction between the adjacent Au NPs (see Figure 2).

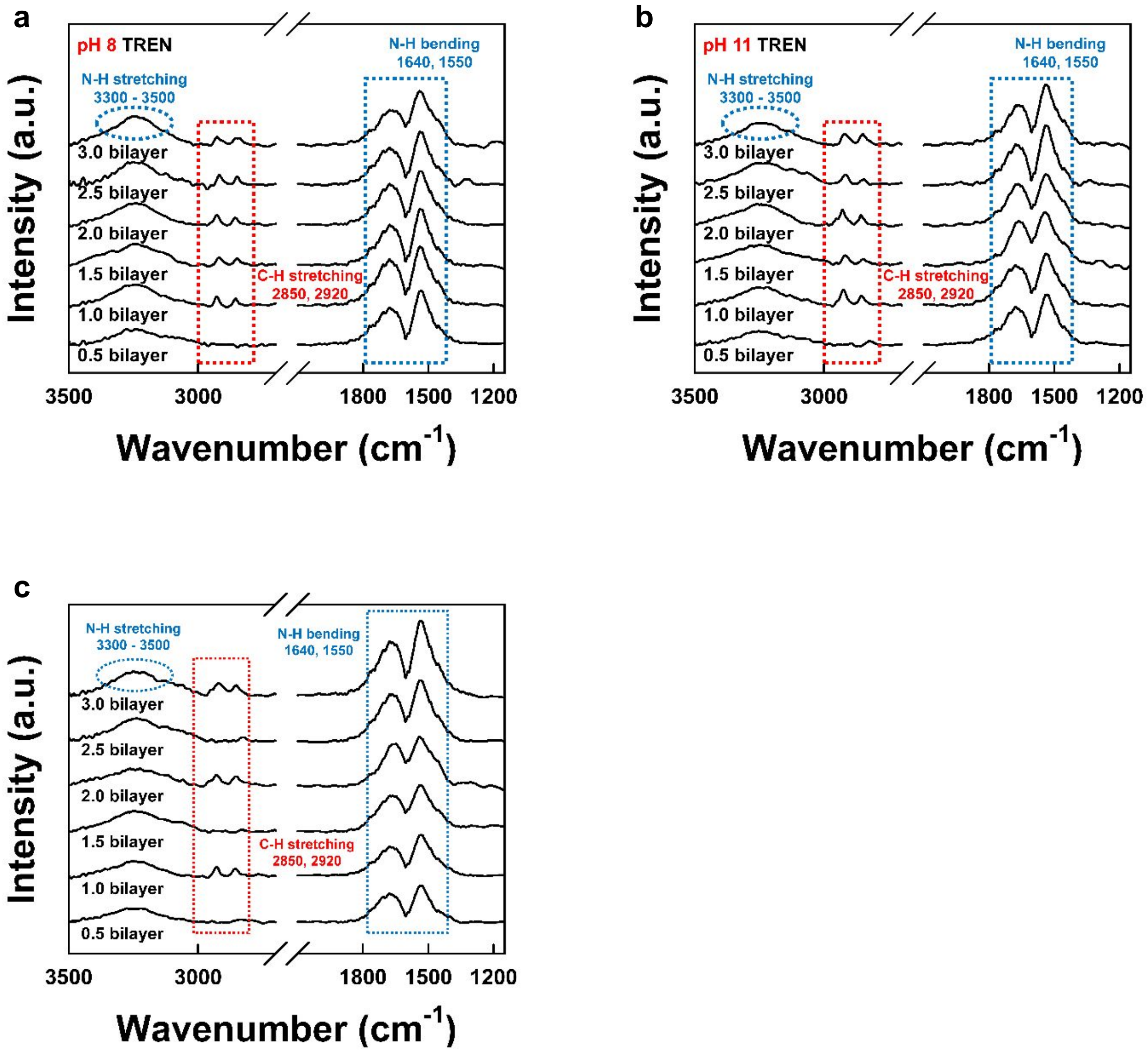

Figure S7. ATR-FTIR spectra of (a) (pH 8 TREN/TOABr-Au NP)$_n$, (b) (pH 11 TREN/TOABr-Au NP)$_n$, and (c) (TREN in ethanol/TOABr-Au NP)$_n$ multilayers as a function of the bilayer number (n).

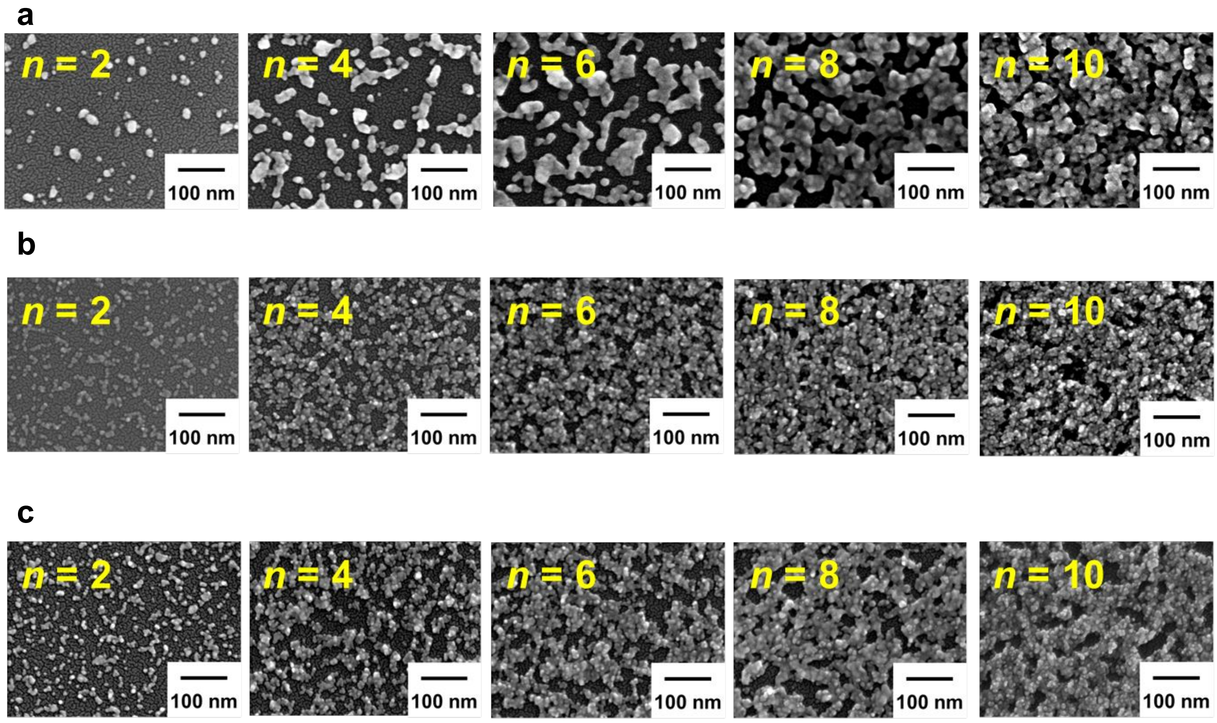

Figure S8. SEM images of (a) (TREN in ethanol/TOABr-Au NP)$_n$, (b) (pH 11 TREN/TOABr-Au NP)$_n$, and (c) (pH 8 TREN/TOABr-Au NP)$_n$ multilayer films with increasing the bilayer number (n) from 2 to 10.

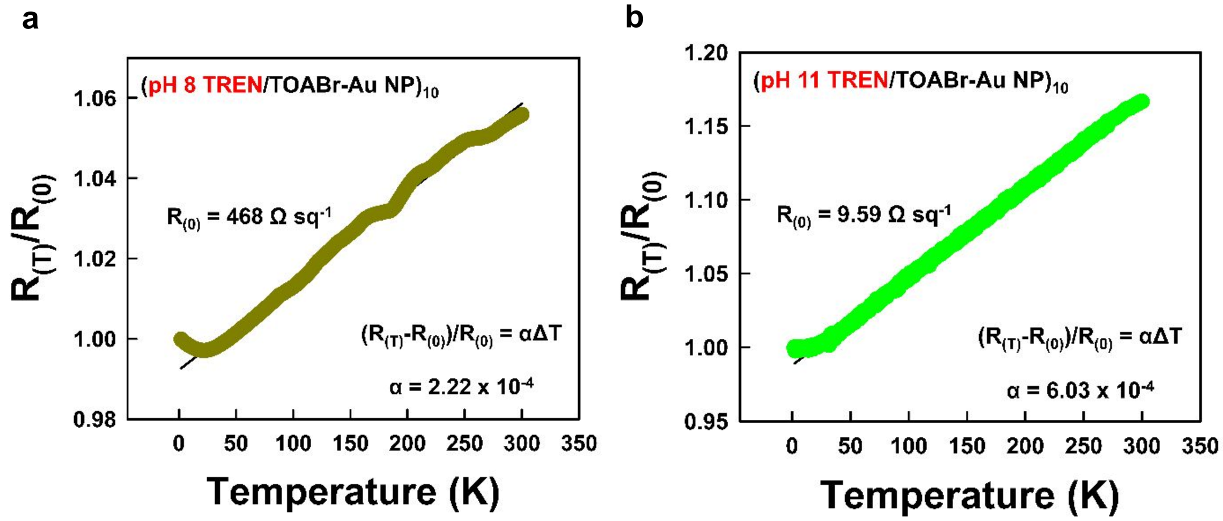

Figure S9. Resistances (($R_{(T)}/R_{(0)}$) vs. temperature (K)) of (a) (pH 8 TREN/TOABr-Au NP)$_{10}$ and (b) (pH 11 TREN/TOABr-Au NP)$_{10}$ multilayers-coated onto quartz glass. As the temperature was decreased from 300 to 2 K, the electrical resistivity of both (pH 11 TREN/TOABr-Au NP)$_{10}$ and (pH 8 TREN/TOABr-Au NP)$_{10}$ multilayers were linearly decreased showing typical metallic conduction behavior. These TREN-based multilayers showed a positive temperature coefficient of 2.22×10^{-4} K^{-1} and 6.03×10^{-4} K^{-1}, respectively. In this case, temperature coefficient was obtained by following equation: $\Delta R_T/R_0 = \alpha\Delta T$, where ΔR_T (i.e., $(R_T\text{-}R_0)/R_0$, where R_T and R_0 are resistance at temperature T and 2 K, respectively) and α are the resistance (Ω) and the temperature coefficient, respectively.

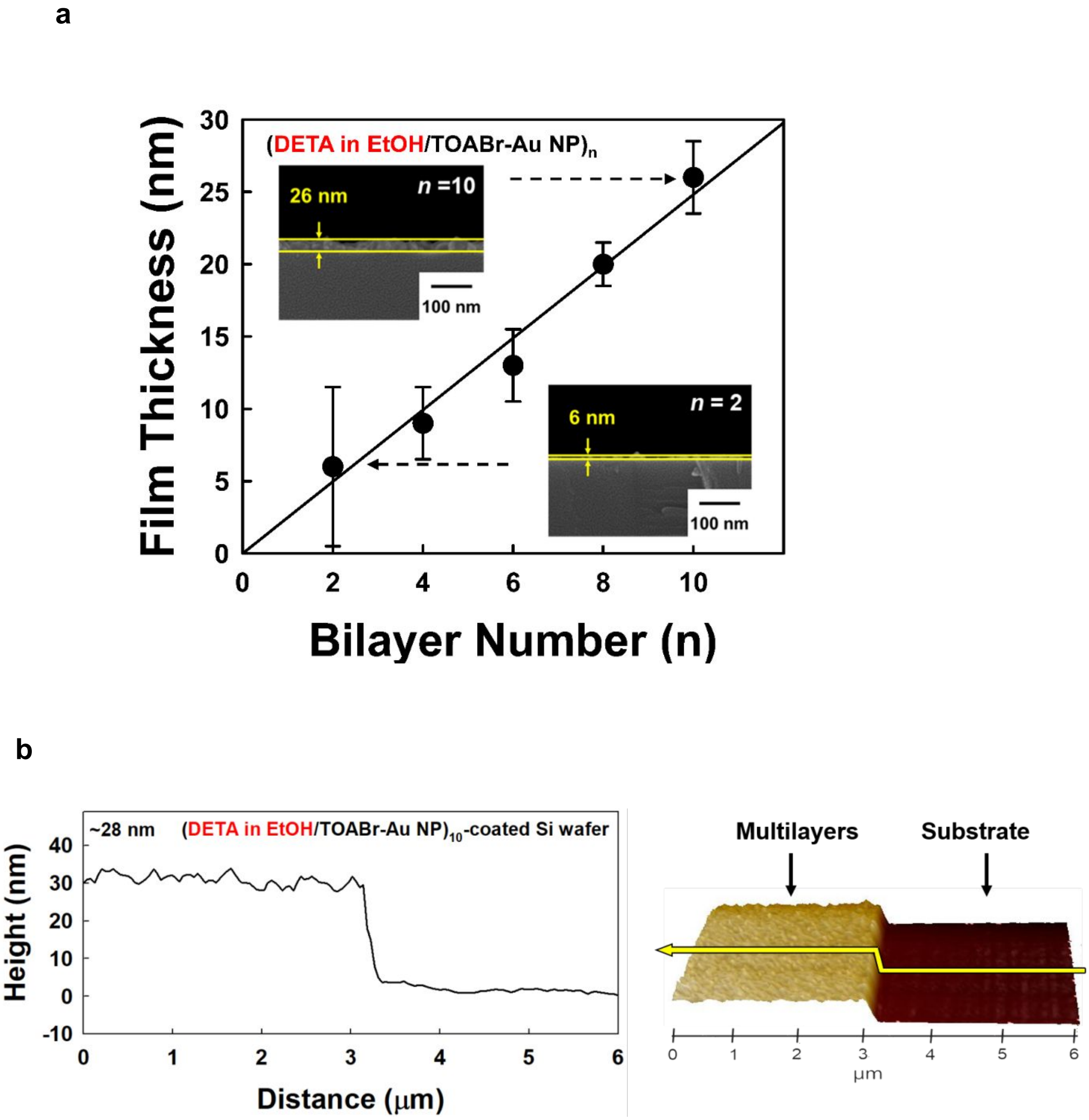

Figure S10. (a) Thicknesses of (DETA/TOABr-Au NP)$_n$ multilayers as a function of the bilayer number (n). The inset shows the cross-sectional FE-SEM images of multilayers. (b) Thickness of (DETA/TOABr-Au NP)$_{10}$ multilayers measured from atomic force microscopy (AFM). The difference of the thickness of (DETA/TOABr-Au NP)$_{10}$ multilayers measured from SEM and AFM is negligible.

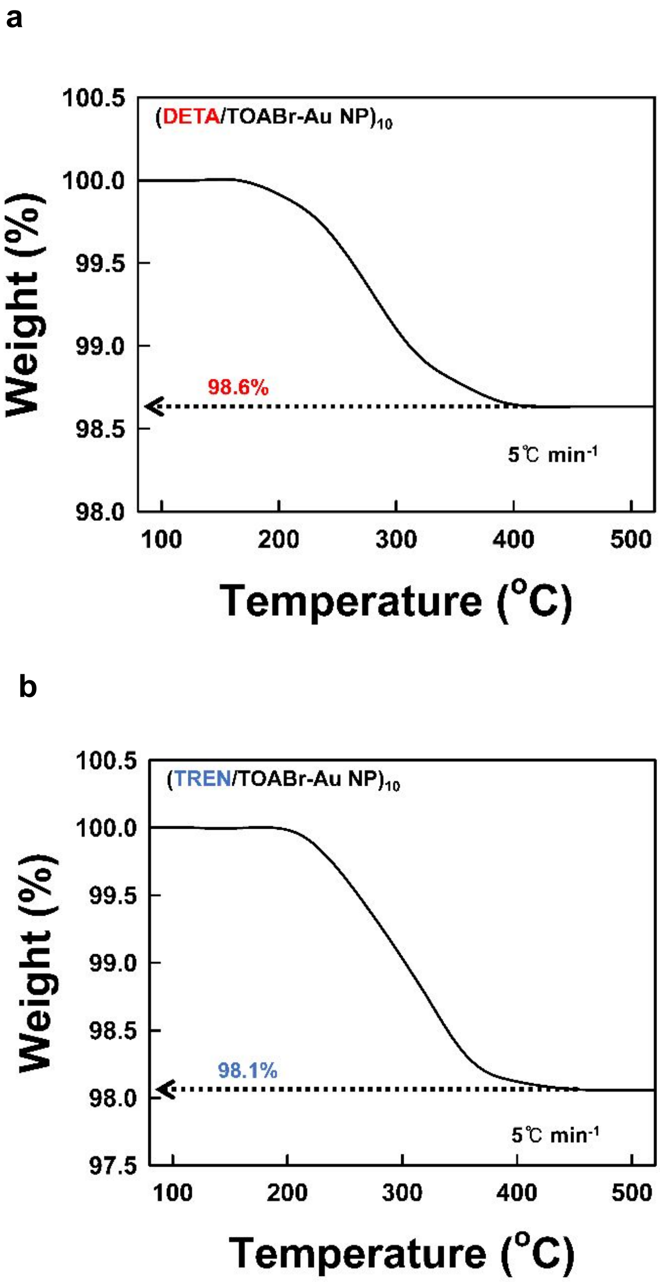

Figure S11. TGA data for the (a) (DETA/TOABr-Au NP)$_n$ and (b) (TREN/TOABr-Au NP)$_n$ multilayer films.

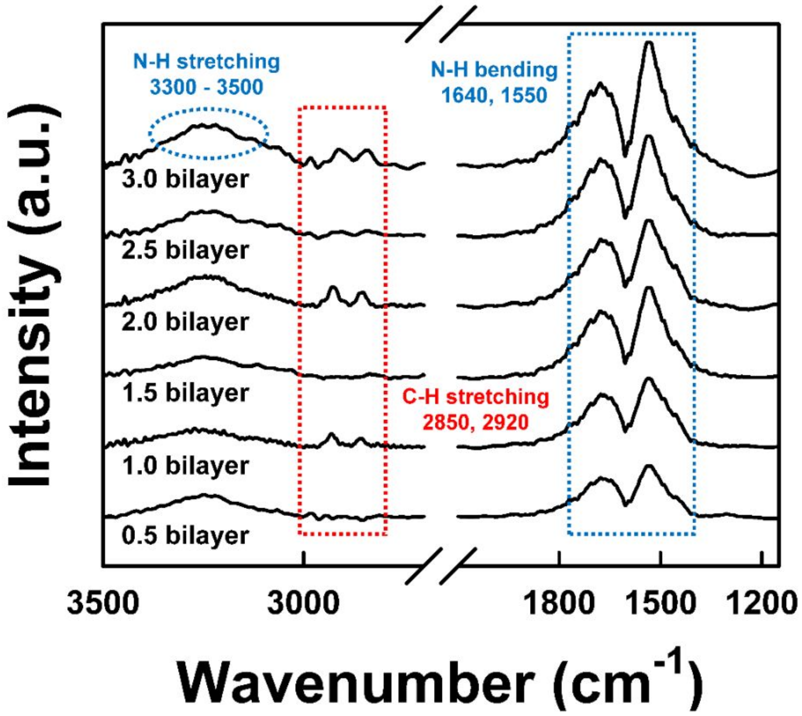

Figure S12. ATR-FTIR spectra of (DETA/TOABr-Au NPs)$_n$ multilayers as a function of the bilayer number (n).

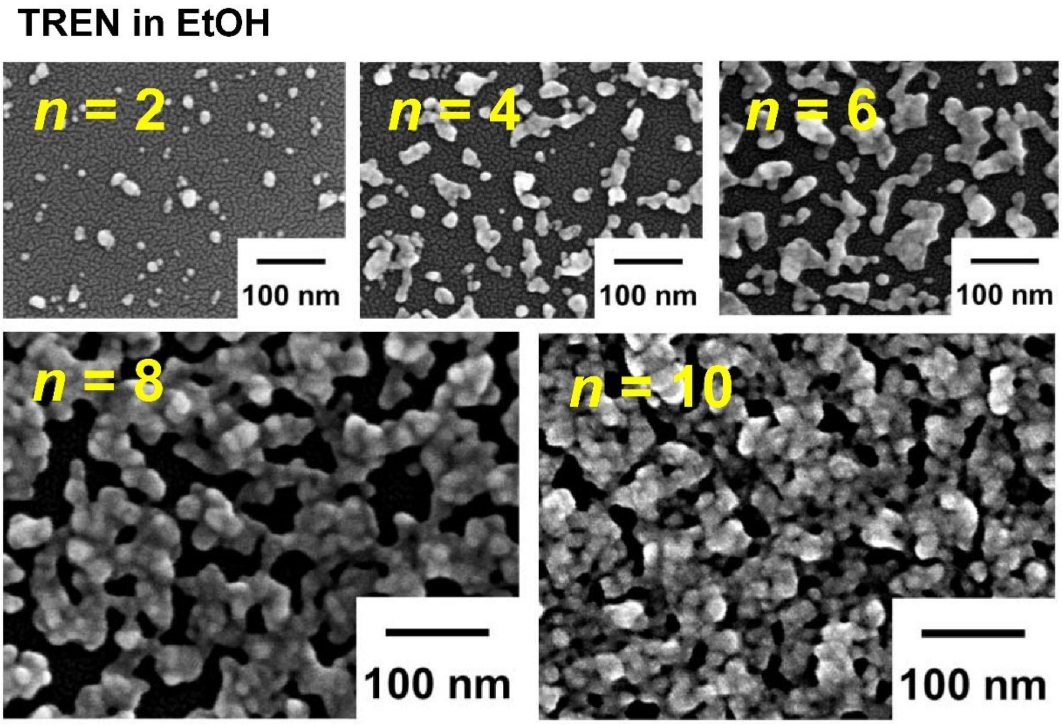

Figure S13. FE-SEM images of (TREN/TOABr-Au NP)$_n$ multilayers with increasing the bilayer number (n).

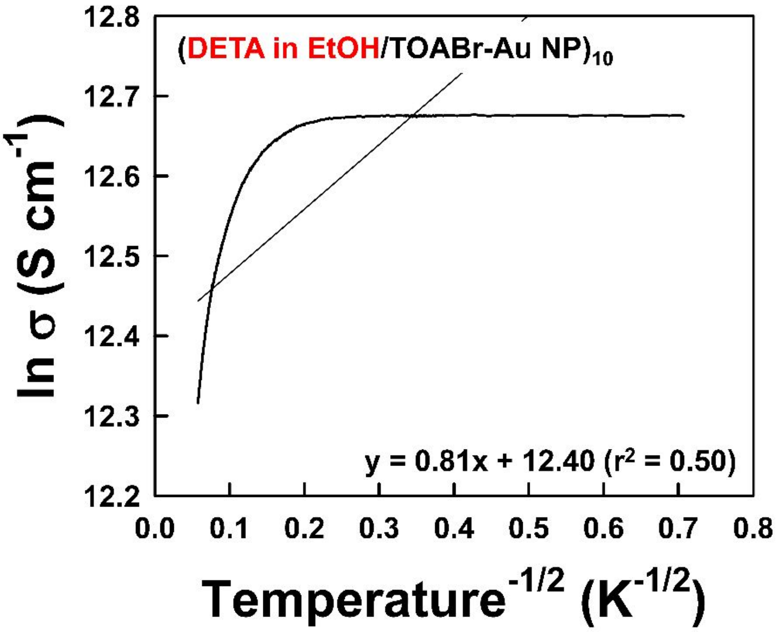

Figure S14. Plots of *ln*σ *vs* $T^{-1/2}$ for the tunneling mechanism of (DETA/TOABr-Au NP)$_{10}$ multilayer films. In this case, the conductivity ($ln\ \sigma$) as a function of $T^{-1/2}$ (for tunneling) for these multilayers does not follow a linear dependence.

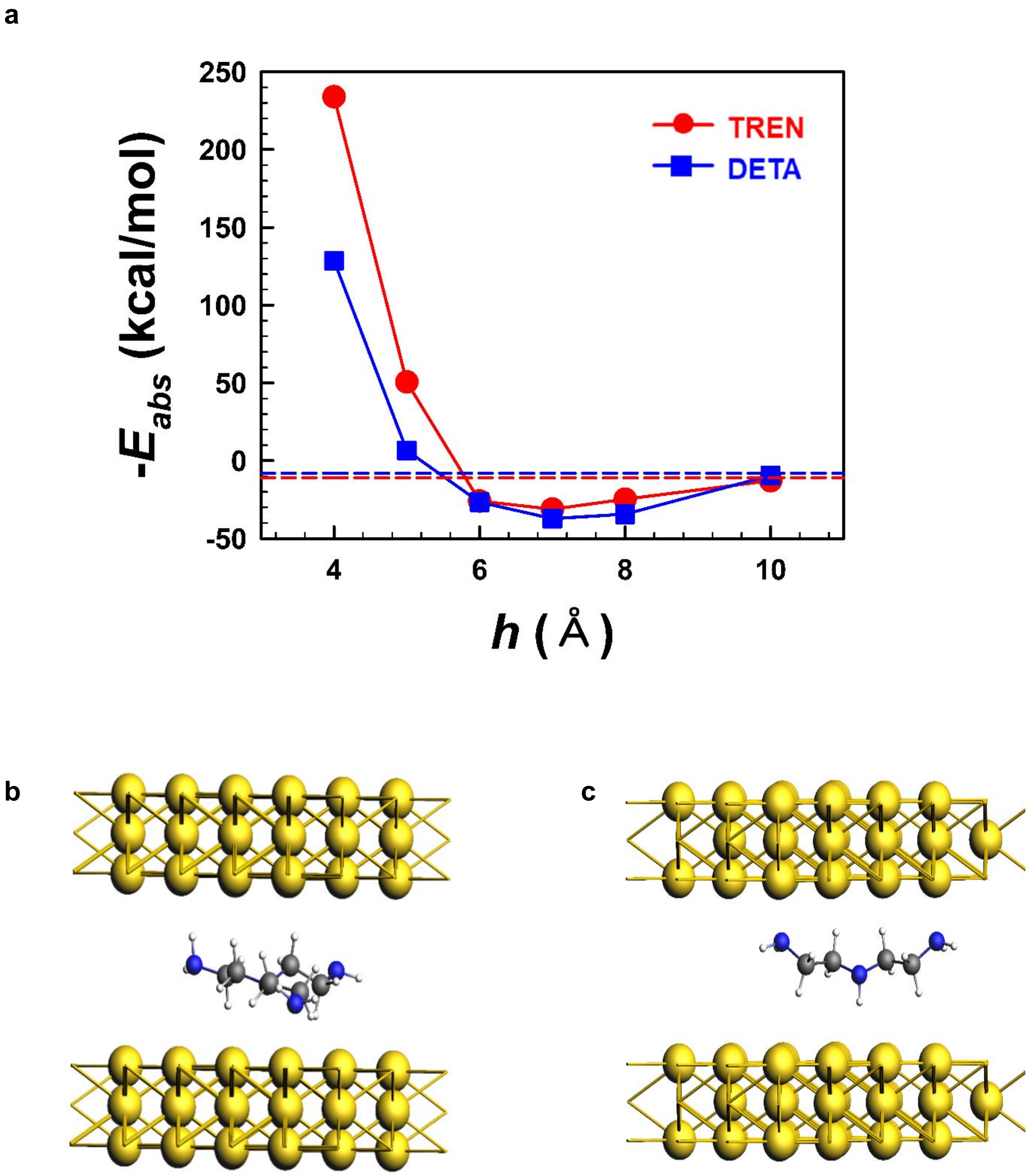

Figure S15. (a) DFT-computed adsorption energy (E_{abs}) of organic linkers between Au surfaces as a function of separation distance (h). The red and dashed lines represent the adsorption energies of TREN and DETA on the single Au surface, respectively. Geometry-optimized molecular structures of (b) TREN and (c) DETA at the separation distance h = 7Å.

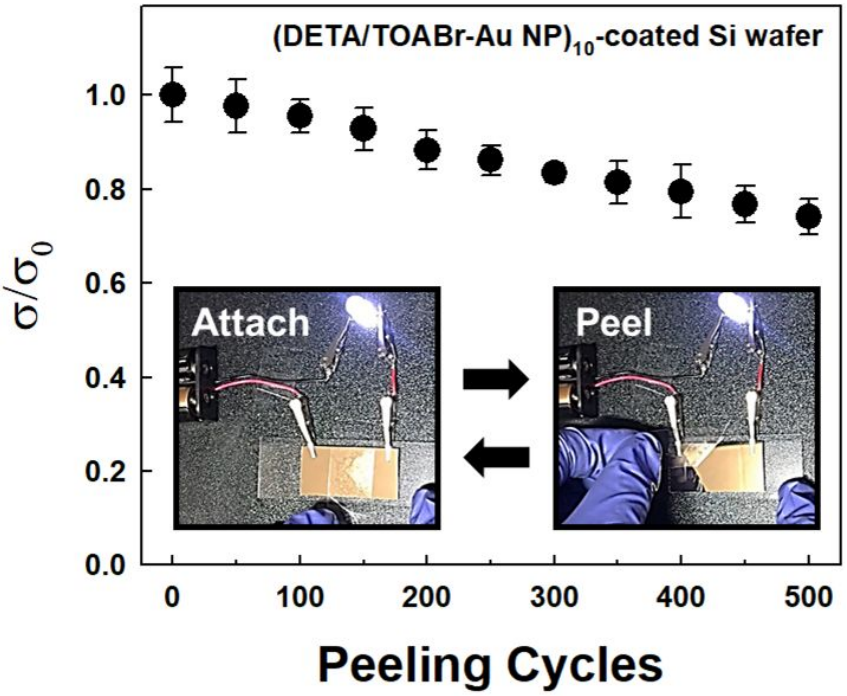

Figure S16. Peeling test of (DETA/TOABr-Au NP)$_n$ multilayer-coated Si wafer using scotch tape. After the peeling tests of 500 cycles, the electrical conductivity (σ) of multilayers maintained 73 % of initial conductivity (σ_0).

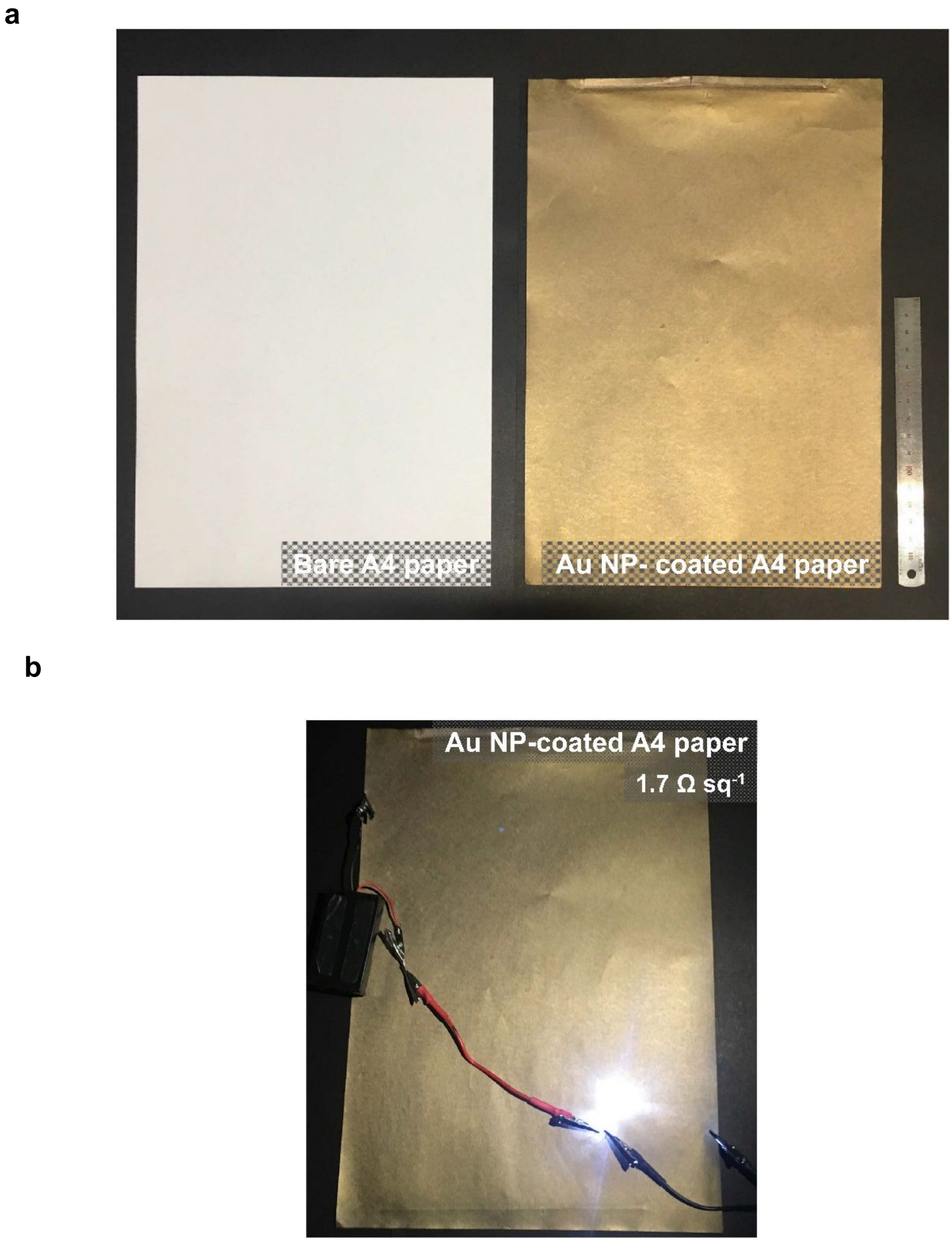

Figure S17. Photographic images of (a) a bare A4 paper (29.7cm x 21.0cm) and a (DETA/TOABr-Au NP)$_{10}$ multilayer-coated (29.7cm x 21.0cm) A4 paper and (b) a LED connected through the (DETA/TOABr-Au NP)$_{10}$ multilayer-coated A4 paper.

Supporting Table S1. Electrical property comparison of metal and carbon-based electrodes.

	Material	**method**	**Resistance ($\Omega\cdot sq^{-1}$)**	**Conductivity ($S\cdot cm^{-1}$)**	**Ref.**
Metal Nanomaterial	Au NP	Layer-by-layer assembly	1.7	2.2×10^5	**Our work**
	Pt NP	Self-assembly Pyrolysis	-	2.5×10^{-3} 400 (pyrolysis)	2
	Au NP	the Langmuir-Blodgett method	-	5.0×10^{-3}	6
	Au NP	Layer-by-layer assembly	-	1.1×10^4	17
	Ag NW	Vacuum filtration	< 10	5.0×10^4	19
	Cu	Electroless deposition	-	1.6×10^5	54
	Cu	Electroless deposition	0.01	1.0×10^3	55
	Ag flake	Stencil printing	-	738	56
	Cu NW/NP	Flash light-sintering	-	4.4×10^4	57**
Carbon-based material	MXene	Spin coating	-	9.9×10^3	58
	SWNT	Dip-coating	-	57	59
	Graphene	Chemical vapour deposition	280	-	60
	CNT forest	Drop-casting	-	0.5 – 1.0	61
	SWNT	Dip-coating	< 1	125	62
	Graphene	Roll-to-roll production Wet chemical doping	125 30 (doping)	-	63

*** PDMS: poly(dimethylsiloxane)**

**** Electrical conductivity was evaluated from given data in the literature.**